09

On the correct use of refractive lenses for microscopy with high spatial resolution at fourth-generation synchrotron radiation facilities

© Yu.V. Khomyakov,[1] Ya.V. Rakshun,[1,2] V.A. Chernov[1]

[1] Budker Institute of Nuclear Physics, Siberian Branch, Russian Academy of Sciences, 630090 Novosibirsk, Russia
[2] Siberian State University of Telecommunications and Information Science, 630102 Novosibirsk, Russia
e-mail: yu.v.khomyakov@yandex.ru

Received April 25, 2024
Revised April 25, 2024
Accepted April 25, 2024

The concept of an undulator-based beamline for refractive lenses-based hard X-ray coherent nanoscopy and nanotomography at a fourth-generation synchrotron radiation source is presented. We describe experimental scenarios and optics operational modes that allow varying the scale of the sample area under study in the range of $\sim 0.1-100\,\mu$m and achieving spatial resolution down to ~ 10 nm. Solutions to eliminate the disadvantages of beryllium lenses are proposed.

Keywords: X-ray microscopy, coherent imaging, synchrotron radiation, X-ray refractive optics.

DOI: 10.61011/TP.2024.07.58812.134-24

Introduction

The emergence of third-generation synchrotron radiation (SR) sources has given rise to extensive development of X-ray coherent diffraction visualization methods. In particular, X-ray ptychographic microscopy ensuring resolution down to ~ 10 nm have got wide applications over the recent 10 years [1,2]. When examining a sample by the ptychographic methods using third-generation SR sources, the problem is in low coherent photon flux resulting in considerable time required to perform scanning. This problem becomes especially acute in high-resolution mapping of relatively large samples and in ptychographic tomography.

Transition to fourth-generation SR sources provides significant brilliance growth and, therefore, makes the coherent examination methods more attractive. And increase in radiation flux density and the coherent fraction results in tightening of requirements for optical elements of SR facility beamlines. Thus, for example, it is difficult to make use of standard beryllium compound refractive lenses (CRL) made by powder metallurgy methods [3] because spurious interference resulting from high transverse radiation coherency [4] is added to the typical contrast deterioration of such lens due to small-angle X-ray scattering [4]. It should be taken into account that at the fourth-generation SR facilities with a relatively low electron energy of 3 GeV high undulator harmonics are used for hard X-ray experiments. In this case, the first optical elements of a beamline are exposed to heat loads with high power density — the first most intense „long-wavelength“ harmonics of the undulator are absorbed.

One of the existing solutions is to use focusing grazing-incidence reflective optics that is mainly used, for example, in microscopy with record-breaking high resolution on beamlines at MAX-IV [5] and SIRIUS [6] facilities. Though the mirror optics is well proven, this solution is the most expensive of all possible. The paper describes a concept of an undulator beamline at the fourth-generation SR facility for coherent X-ray microscopy based on refractive optics, and proposes solutions neutralizing the disadvantages of X-ray lens in ptychography.

1. Optical arrangement and operation modes

Short-period superconducting undulators installed in the diffraction-limited storage rings of the modern SR sources open up a number of opportunities for hard X-ray coherent high-resolution microscopy and microtomography. Implementation of the fourth-generation SR source potential is a challenge for X-ray optics and imposes the following requirements:

- achieve the focus spot size less than 100 nm;
- vary the radiation spot size with retaining its position on the specimen for mapping in different scales;
- perform monochromatization with a spectral width of both $\Delta E/E \sim 10^{-2}$ and 10^{-4};
- minimize the wavefront distortions;
- retain high photon fluxes;
- withstand thermal loads with high power density;
- ensure time stability (including neutralizing electron beam orbit oscillations influence).

The authors propose a beamline concept satisfying the requirements listed above; the appropriate optical arrangement is shown in Figure 1. SR beam generated by the undulator first flows through the primary filters, its angular sizes are defined by the fixed and adjustable frontend masks. Then,

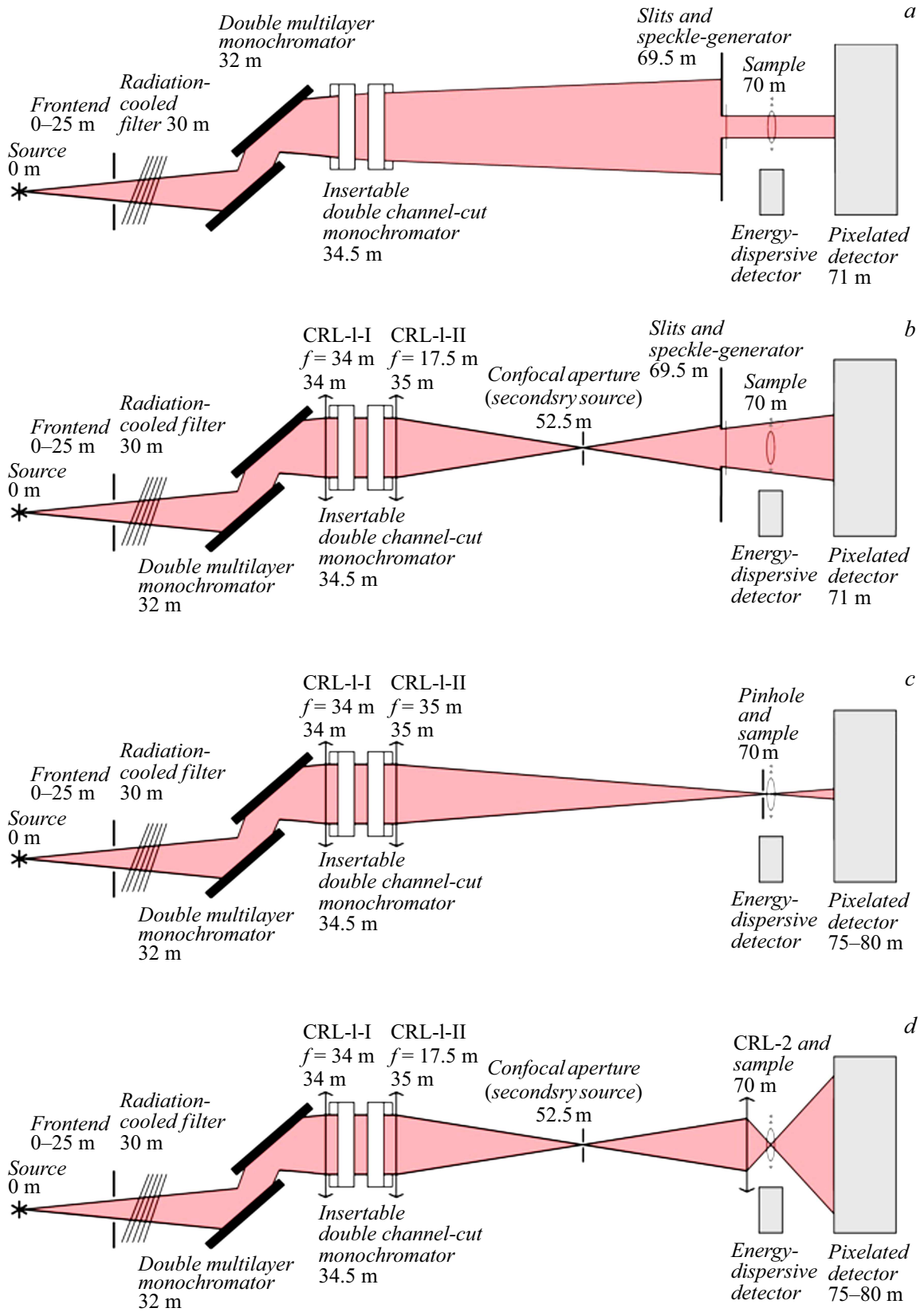

Figure 1. Optical arrangement of the beamline (plan view): *a* and *b* — speckle microscopy mode (lensless and with secondary source, respectively), spot size 0.1–1 mm; *c* — „coarse“ scanning mode, spot size 1–10 μm; *d* — „fine“ scanning mode, spot size 10–100 nm.

the radiation falls onto a radiation-cooled filter that consists of a set of X-ray amorphous multilayer thin films and serves for absorption of spurious low-energy photons. Primary monochromatization with $\Delta E/E \sim 10^{-2}$ of filtered radiation is performed using double-mirror multilayer monochromator (DMM). DMM also ensures reduction of thermal load on the following optical elements. If required, additional monochromatization with $\Delta E/E \sim 10^{-4}$ is provided by inserting a double channel-cut monochromator (DCCM) Si(111) retaining the beam center line. This optical arrangement features the use of distributed primary X-ray lenses that are installed upstream and downstream of DCCM.

By inserting and removing X-ray lenses, three microscopy modes can be implemented with retaining the beam position on the specimen.

• The speckle microscopy mode that uses adjustable slits to extract coherent photon flux and a speckle generator (for example, fine-grain abrasive paper) is intended for speckle-based multimodal X-ray imaging. It may be used in lensless option (Figure 1, *a*) or with beryllium lenses (CRL-1) that focus SR beam on a confocal aperture (pinhole) forming a secondary source (Figure 1, *b*). In the option with the secondary source, the transverse coherency length is isotropic and may be adjusted by changing the pinhole diameter. The radiation spot size on the specimen $\sim 100-1000\,\mu$m, resolution $\sim 1\,\mu$m. Pixel detector records the intensity distribution in the Fresnel diffraction mode. It is important that the speckle microscopy allows for wavefront distortion by optics significantly reducing requirements for its quality.

• The „coarse“ scanning mode (Figure 1, *c*), where CRL-1 set focuses the SR beam on the pinhole directly upstream of the specimen, is intended for ptychography with the illumination spot size of $1-10\,\mu$m and resolution down to ~ 100 nm. The pixel detector records intensity distribution in the Fraunhofer diffraction mode.

• In the „fine“ scanning mode (Figure 1, *d*), CRL-1 set forms the secondary source on the confocal aperture, and the final focusing is performed by a set of strong adiabatically focusing crossed planar lenses (CRL-2). This mode is intended for ptychography with an illumination spot size of ~ 100 nm and resolution of ~ 10 nm. The pixel detector records intensity distribution in the Fraunhofer diffraction mode.

In all modes, fluorescent signal is recorded to obtain additional data concerning the specimen using the energy-dispersive detector.

CRL-1 set is divided into two parts. CRL-1-I collimates the diverging beam upstream of DCCM that facilitates preservation of the photon flux (see the DuMonde diagrams in Figure 5, *b*). CRL-1-II in turn focuses the quasiparallel beam on the pinhole upstream of the specimen or on the second confocal aperture.

The described configuration with three microscopy modes implies the following experiment scenario.

• First, speckle-based X-ray imaging is used to build a multimodal map of the whole specimen with attenuation, refraction, and small-angle scattering (diffusive-dark-field) signals retrieval [7]. Integral fluorescent signal giving the information about the elemental composition of the specimen is recorded in parallel. This step is also applicable to *in situ* studies [8,9].

• Then by moving the specimen in plane, „coarse“ focused-beam scanning is performed over the required (large) area with overlapping the neighboring illuminated zones. From the recorded diffraction patterns, the iterative ptychographic algorithm is used to retrieve the specimen map with high resolution [10]. Simultaneously, these fluorescent spectra are used to build complementary element concentration distribution maps.

• If required, the area of interest is „finely“ scanned similar to the previous step, but with even better resolution.

Precision rotation of the specimen with retrieval of its projection images by the speckle-based imaging and ptychography methods is used to build high-resolution 3D maps [11,12]. And the SR beam stability during scanning is ensured by slits (Figure 1, *a*), pinholes upstream of the specimen (Figure 1, *c*) or confocal aperture (Figure 1, *b, d*).

2. Calculation parameters

Parameters of the SKIF storage ring [13] and parameters of the Microfocus beamline superconducting undulator [14] were taken for optical calculations and thermal load estimates, see Table 1. It is important that SKIF accommodates a beamline with a length up to 80 m on a single foundation, and this defines the positions of detector, specimen and X-ray optical elements as shown in Figure 1. Note that the source was extended horizontally and its aspect ratio is approximately equal to 8 : 1.

The calculations assumed that the beamline frontend uses masks to set the angular aperture $(75\,\mu\text{rad})^2$, and also use carbon filters with density $\rho = 2.25\,\text{g/cm}^3$ and total thickness $1200\,\mu$m.

3. Filters

When used in the hard X-ray range, the undulator beamlines of fourth-generation SR sources with a relatively low electron energy face an acute problem of thermal power removal and thermal stabilization of the first optical elements. Therefore, there is a need to suppress unused high-intensity low-energy undulator harmonics.

For this, a heat-resistant radiation-cooled X-ray amorphous filter is proposed. The filter consists of a thin multilayer film package placed downstream of the shield wall. Such filter will absorb the low-energy portion of spectrum and, thus, will reduce considerably the thermal load on the following optical elements without introducing wavefront distortions.

Figure 2, *a* shows spectrum of the photon flux emitted into a solid angle of $(75\,\mu\text{rad})^2$ upstream of filters, downstream of the carbon filter $1200\,\mu$m, downstream of DMM

Table 1. storage ring and superconducting undulator parameters used for calculations

Parameter	Value
Storage ring	
Electron energy, GeV	3
Beam current in the main mode, mA	400
Horizontal beta-function in the center of the straight section, m	15.6
Vertical beta-function in the center of the straight section, m	2.4
Horizontal emittance in the main mode (with full current), pm·rad	68.18
Vertical emittance in the main mode (with full current), pm·rad	6.818
Horizontal electron bunch size in the center of the straight section $\sigma_x = \mathrm{FWHM}_x/2.355$, μm	32.6
Vertical electron bunch size in the center of the straight section $\sigma_y = \mathrm{FWHM}_y/2.355$, μm	4.02
superconducting undulator	
Period, mm	15.6
Peak magnetic field, T	1.25
Number of periods	128

(in this example, DMM is set to transmission of 30.9 keV) and downstream of DMM with introduced additional SiC filter with a total thickness of 300 μm. The required thickness of SiC is provided by the SiC/Be multilayer film package. When used at high energies, the DMM mirrors are placed at grazing angles $\sim 0.5^\circ$ to the beam due to which DMM transmits low-energy harmonics of the undulator as a result of total external reflection phenomenon (see the DuMonde diagrams in Figure 3, *a*). Additional SiC 300 μm filter ensures suppression of these spurious harmonics reducing considerably the thermal load on the first crystal of DCCM.

The undulator radiation power downstream of the front-end at the fourth-generation SR source beamlines achieves hundreds of W, however, all this power is concentrated within a small solid angle of about $(100\,\mu\mathrm{rad})^2$. Thus, the filter must withstand conditions of extremely high local thermal load.

To ensure that the surface density of the absorbed power does not exceed the allowable limit [15], in this case the SiC layer thickness within the first film shall not exceed 1 μm. Efficiency of the radiative heat sink is ensured by spacing individual films at several millimeters. To make the device more compact, film thicknesses may be increased as the SR beam goes through the filter unit and is attenuated. The calculated map of SR power density absorbed by the first film of the filter unit in case of normal incidence is shown in Figure 2, *b*.

3D and 2D densities of the absorbed power and the thermal equilibrium temperature almost do not depend on the angle θ between the film surface and SR beam at $\theta \sim 1$ rad. However, when θ decreases, the effective filter thickness increases by a factor of $1/(\sin\theta)$ which is equivalent to the same decrease in the required number of films. The calculated map of SR power density absorbed by the first film of the filter unit at angle $\theta = 10^\circ$ is shown in Figure 2, *c*. It is difficult to use filtering films at grazing angles ($\sim 1^\circ$) because the heat-induced deformation effects become significant. This case will be described in detail in a separate paper.

4. Multilayer monochromator

The next optical element on the way of SR beam is DMM. DMM serves for primary monochromatization and reduction of thermal load on the downstream optical elements. In addition, DMM ensures parallel offset of the SR beam by separating it from gamma quanta generated as a result of electron scattering by residual gas in the storage ring. During operating energy rearrangement and corresponding change in the grazing angle, the second mirror moves along the beam in such a way as to ensure constant offset.

To ensure DMM functioning within the energy range of 10–31 keV, three strips of multilayer coatings have been chosen and their parameters are shown in Table 2. When using Mo/B_4C and W/B_4C coatings [17], the relative energy acceptance of DMM $\Delta E/E$ is 10^{-2} which corresponds to transmission of one undulator harmonic; and DMM is used together with DCCM. Cr/Be coating [18] with $\Delta E/E = 0.4 \cdot 10^{-2}$ may be used for „pink“ beam operation, i.e. without DCCM. DuMonde diagrams for DMM are shown in Figure 3, *a*.

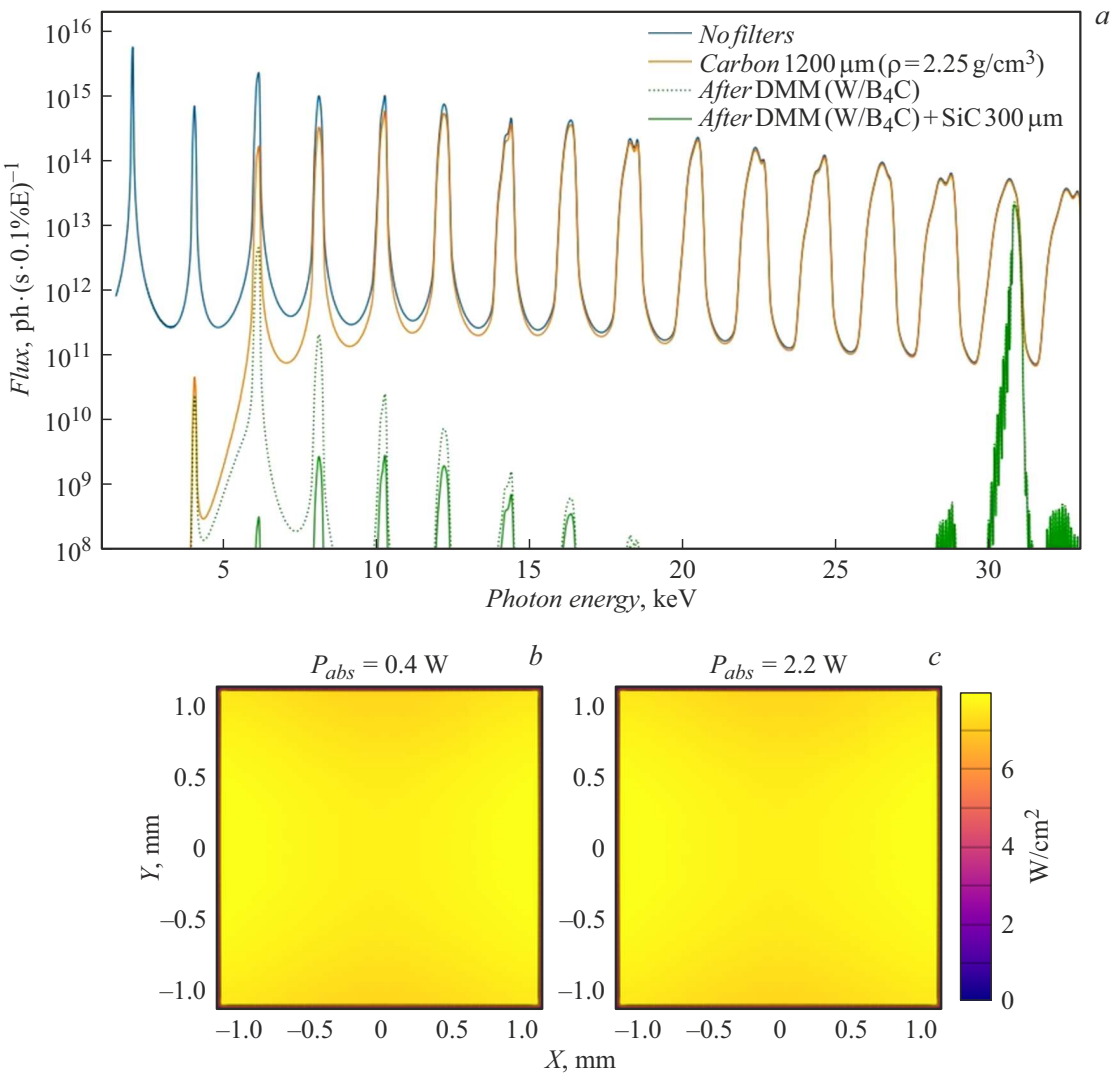

Figure 2. Radiation-cooled filter: *a* — attenuation of spurious „soft“ harmonics; *b* and *c* — maps of radiation power density absorbed by the SiC 1 μm film in cases of normal incidence and incidence at angle $\theta = 10^\circ$ to the surface, respectively. The calculation was performed using SPECTRA [16].

Table 2. DMM parameters

Parameter	Value
Mirror length	200 mm
Axis of rotation	vertical
Coating 1 (multilayer, number of periods N, period d, high-Z layer thickness vs. period β, RMS interlayer roughness σ)	Mo/B_4C, $N = 300$, $d = 3.83$ nm, β=0.22, σ_{Mo}=0.3 nm, σ_{B4C}=0.3 nm
Coating 2 (multilayer, number of periods N, period d, high-Z layer thickness vs. period β, RMS interlayer roughness σ)	W/B_4C, N=300, d=2.1 nm, β=0.38, σ_W=0.25 nm, σ_{B4C}=0.49 nm
Coating 3 (multilayer, number of periods N, period d, high-Z layer thickness vs. period β, RMS interlayer roughness σ)	Cr/Be, $N = 400$, $d = 2.39$ nm, $\beta = 0.43$, $\sigma = 0.43$ nm

Calculated distribution of the surface power density of radiation falling onto the first mirror of DMM for the most thermally loaded case (set to 10.3 keV, grazing angle 0.927°) is shown in Figure 3, *b*. The peak density achieves 0.46 W/mm^2, the corresponding full power is 158 W. It was shown in [19] that the double-mirror

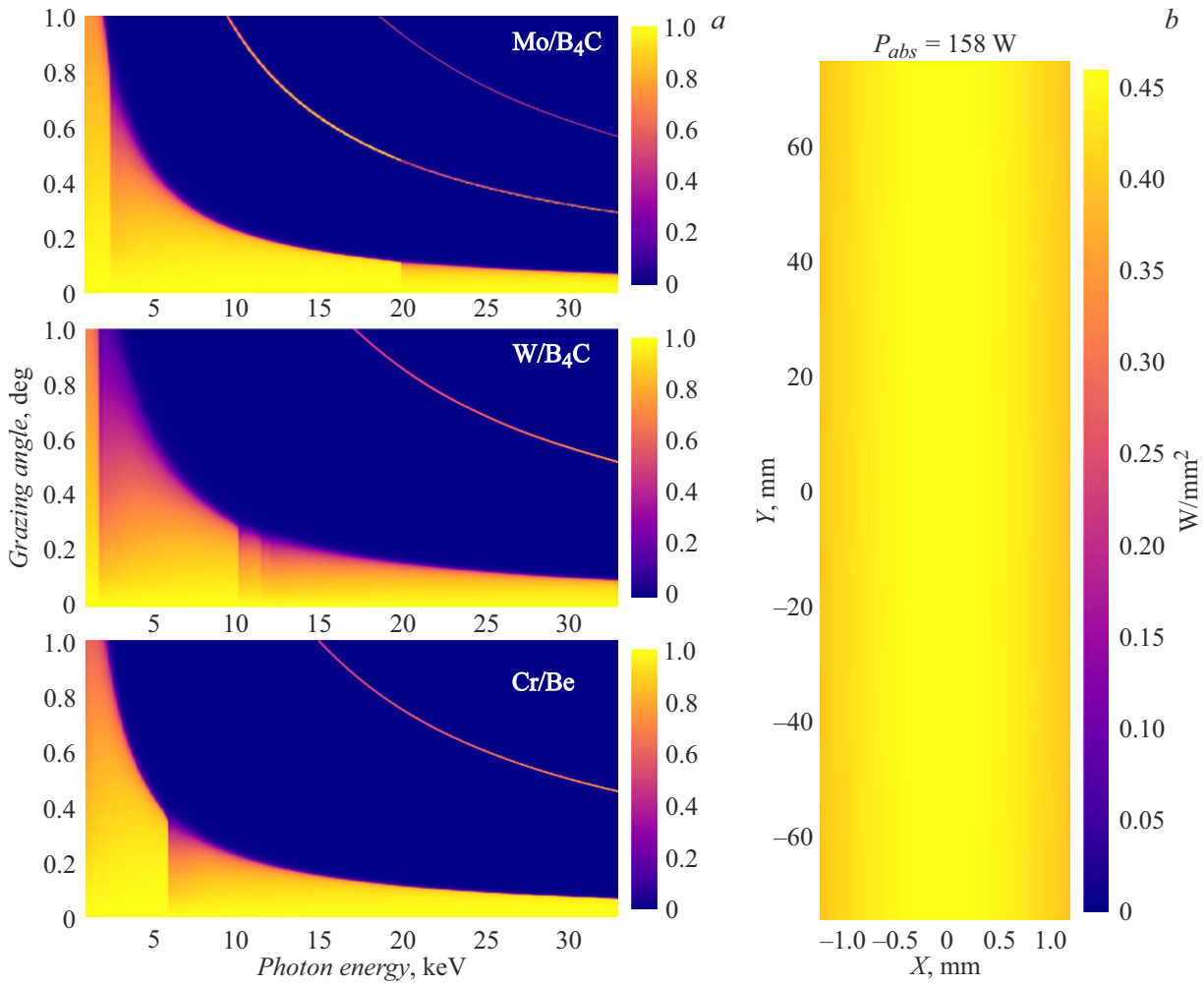

Figure 3. Double-mirror multilayer monochromator: *a* — DuMonde diagrams (coating materials are specified, DMM transmittance is color-coded); *b* — map of surface density of radiation power falling on the first mirror of DMM.

multilayer monochromator on silicon single-crystal substrate accepting inherently higher thermal loads may function with water cooling.

5. First set of lenses

The first set CRL-1 is placed downstream of the DMM unit. The set is divided into two parts: CRL-1-I at 34 m from the undulator center has a focal distance of 34 m and collects radiation into a quasiparallel beam, CRL-1-II at 35 m with a focal distance of 35 m or 17.5 m focuses radiation on the pinhole upstream of the specimen at 70 m or on the confocal aperture at 52.5 m, respectively. CRL-1 material is beryllium, radii of curvature are $R = 0.5$ and 5 mm. The calculated map of two-dimensional density of absorbed power in the most thermally loaded mode (DMM is set to 10.3 keV) for the first lens with $R = 500\,\mu$m is shown in Figure 4, *a*.

Powder beryllium porous lenses result in small-angle X-ray scattering (SAXS) and emergence of spurious speckle structures on the undulator beamlines of the next generation sources due to partial coherency [3,4]. Nevertheless, beryllium is a widely used material for X-ray lenses due to high δ/β ratio, it is quite low-cost in use.

6. Crystal monochromator

For the final monochromatization with $\Delta E/E \sim 10^{-4}$, the „double channel-cut“ monochromator is inserted into the beam. This is a mirror symmetric pair of Si(111) „channel-cut“ monochromators with beam path in the vertical plane (Figure 5, *a*). Such configuration automatically implements the zero-offset fixed-exit.

The pair of „channel-cut“ crystals improves the energy resolution, and the resultant angular acceptance of the monochromator is reduced significantly (see the DuMonde diagrams in Figure 5, *b* right and central). Therefore, to keep the photon flux in the ptychography mode and speckle microscopy mode with the secondary source, DCCM is

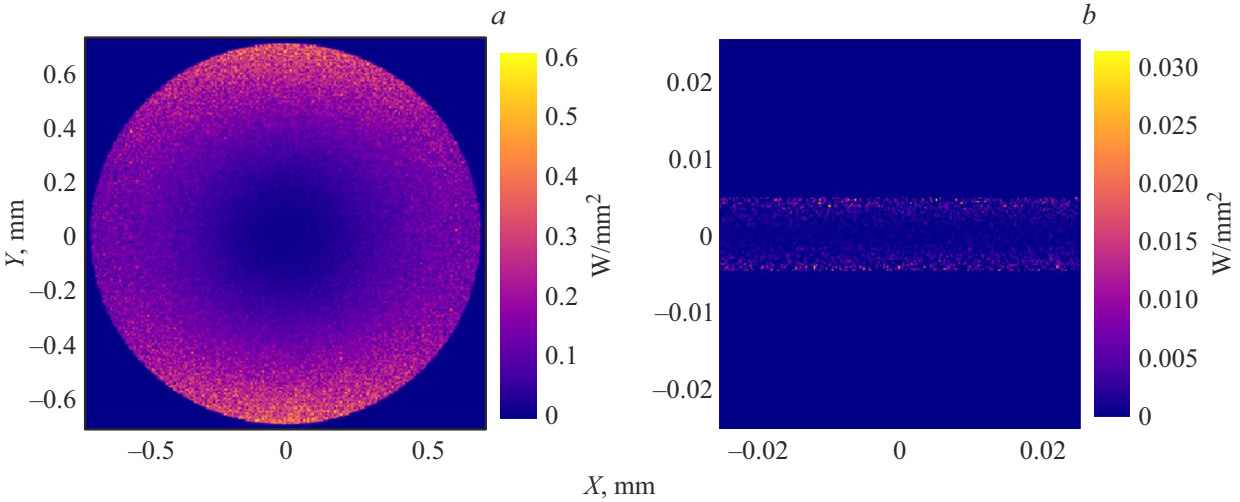

Figure 4. Absorbed power maps: *a* — for the first lens of CRL-1-I; *b* — for the first lens of CRL-2.

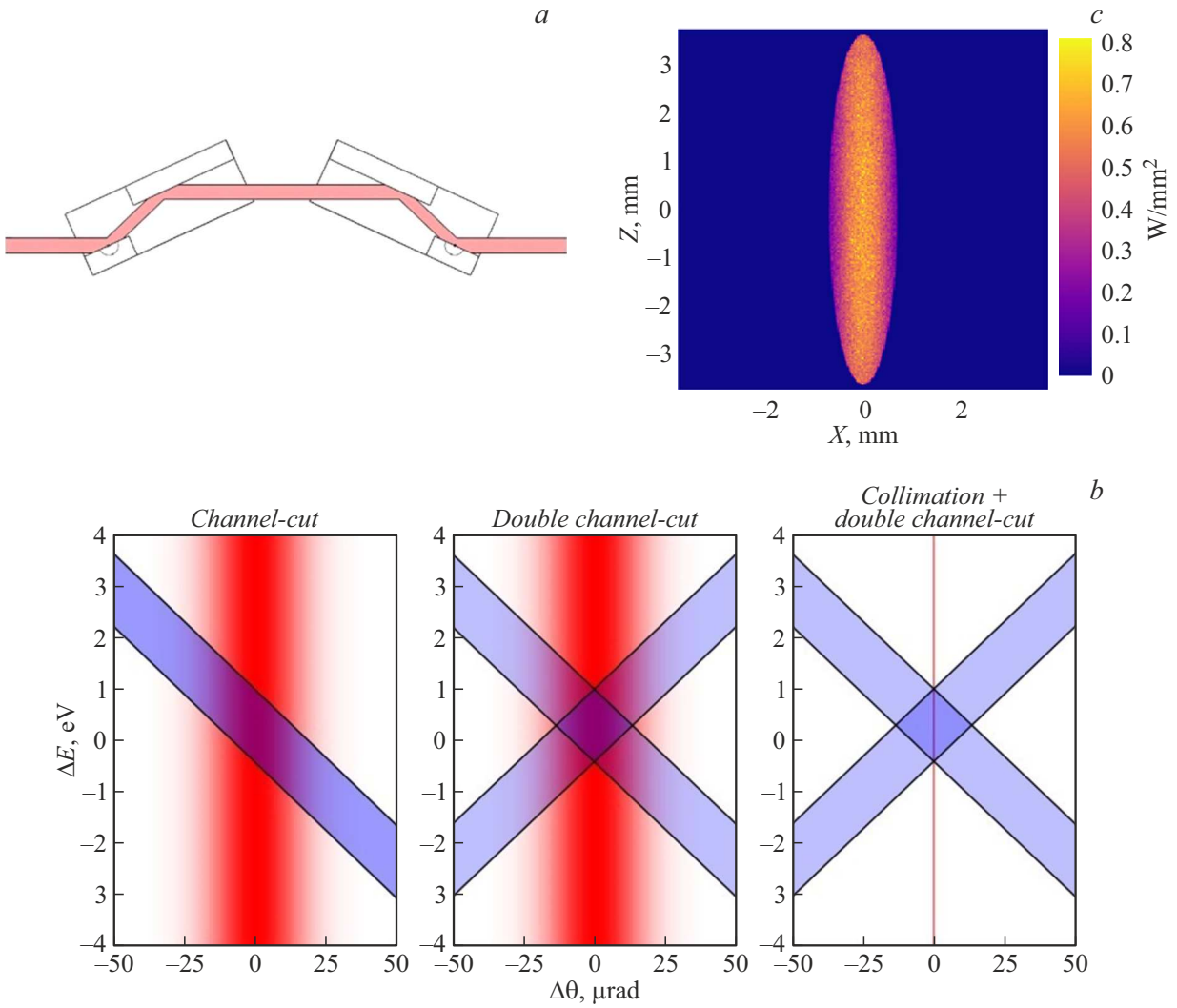

Figure 5. „Double channel-cut“ monochromator: *a* — beam path (side view); *b* — DuMonde diagrams with setting to 10307 eV, red — angular extent of the beam, blue — crystal acceptance; *c* — map of absorbed power on the first lamella.

used together with CRL-1-I collimating set, the right-hand diagram in Figure 5, *b*.

Also note that, when DMM and DCCM are used together, spurious multiple harmonics of monochromators are suppressed together effectively [20]. In this case, DCCM provides the spectromicroscopy possibility: specimen maps are plotted for different energies within one undulator harmonic transmitted by DMM. Energy scanning may be performed, for example, with crossing the absorption edge of elements for their localization on the specimen.

The power density map of radiation absorbed by the first lamella of the first crystal of DCCM in the most thermally loaded case (set to 10.3 keV) is shown in Figure 5, *c*. Density in center achieves 0.75 W/mm^2, the corresponding full power is 3.7 W. It was shown in [21] that the crystal monochromator accepting inherently higher thermal loads may function with water cooling.

7. Second set of lenses

Crossed adiabatically focusing planar lenses made, for example, from Si single-crystal [22] or SU-8 polymer [23] with a focal distance of $f \sim 5$ mm and numerical aperture NA $\sim 10^{-3}$ (CRL-2 in Figure 1, *d*) are proposed as final-focus optics for the „fine“ scanning mode. This optics has no disadvantages of the powder beryllium lenses and has been used for hard X-ray imaging with record-breaking focal spot sizes down to < 20 nm [22]. It is important that the radiation monochromatization and the use of confocal aperture in the intermediate beam focus reduce considerably the thermal and radiation loads on CRL-2 making the polymer lenses potentially suitable for operation. Figure 4, *b* shows the map of absorbed power for a parabolic cylindrical Si lens with a radius of curvature of 2.45 μm and geometrical aperture of 9.4 μm [22].

8. Apertures

In all operation modes, apertures are used downstream of the monochromating optics (and CRL-1, if any). The speckle microscopy mode uses adjustable slits at 69.5 m that extract the coherent photon flux; the pinhole is inserted at 70 m upstream of the specimen in the „coarse“ scanning mode; the confocal aperture (pinhole in the intermediate beam focus) that defines the secondary source shape and size is inserted in the „fine“ scanning mode. All apertures are made of a refractory and highly absorbing material, for example, Ta or W.

Pinholes for ptychography are sets of holes with different outlet diameters (from units to hundreds of μm) in the absorber sheet; discrete variation of the illuminated zone sizes is performed by switching between the operational holes by means of transverse movement of the absorber sheet. The taper of holes prevents the waveguide effect. The pinhole used in the beam focus eliminates the background induced by SAXS in beryllium lenses and provides the aspect ratio of the beam cross section equal to one. Note also that the chromatism of CRL-1 set ensures suppression of higher harmonics of the multilayer monochromator used without DCCM — radiation with a multiple times higher energy turns to be „underfocused“ when going through the pinhole. It is important that pinholes also cancel out beam jitter on the specimen induced by low rocking of the electron beam orbit in the storage ring and also neutralize the wavefront distortions induced by upstream X-ray optical elements, thus, „zeroing the history“ of the SR beam. Thus, the „fine“ scanning mode creates a spectrally pure stable monochromatic high-intensity secondary source with high spatial coherency. Due to this, nanofocusing being provided by specialized final-focus optics becomes possible..

Full beam absorption at 10.3 keV without DCCM is the most thermally loaded case for apertures. The corresponding power and peak power density of absorbed radiation for lensless microscopy, „coarse“ and „fine“ scanning modes are listed in Table 3.

9. Radiation on the specimen

Transverse and longitudinal coherency lengths $l^{(trans)}$ and $l^{(long)}$ are important properties of radiation on the specimen. At the specified calculation parameters at 10.3 keV, we have

$$l^{(long)} = \frac{\lambda^2}{2\Delta\lambda} \approx \begin{cases} 6\,\text{nm}, & \text{if only DMM} \\ 600\,\text{nm}, & \text{if DCCM is inserted} \end{cases}.$$

For the lensless option of the speckle microscopy mode:

$$l_{x,y}^{(trans)} = \frac{\lambda R}{2\sqrt{\pi}\sigma_{x,y}} \approx \begin{cases} 72\,\mu\text{m} & \text{along } x \\ 420\,\mu\text{m} & \text{along } y \end{cases},$$

for the option with a secondary source the sizes of which are defined by the pinhole diameter at $D = 5\,\mu$m:

$$l_{x,y}^{(trans)} = \frac{\lambda R}{2D} \approx 210\,\mu\text{m}.$$

Transverse coherency lengths in the specimen plane correspond to transverse sizes of the imaged area in the speckle microscopy mode. Note that the speckle-based X-ray imaging has relatively low requirements for spatial coherency and also may be performed using polychromatic radiation [24,25].

Figure 6 shows calculated cross sections of the SR beam on the specimen at 10.3 keV in the lensless speckle microscopy mode (*a*), secondary source speckle microscopy mode (*b*) and „coarse“ scanning mode (*c*); estimated photon fluxes and corresponding powers, FWHM sizes of the illuminated zone, and spectra are shown. In the speckle microscopy mode, radiation spot sizes are set by the adjusted slits upstream of the specimen (corresponding coherency length are taken for the calculation).

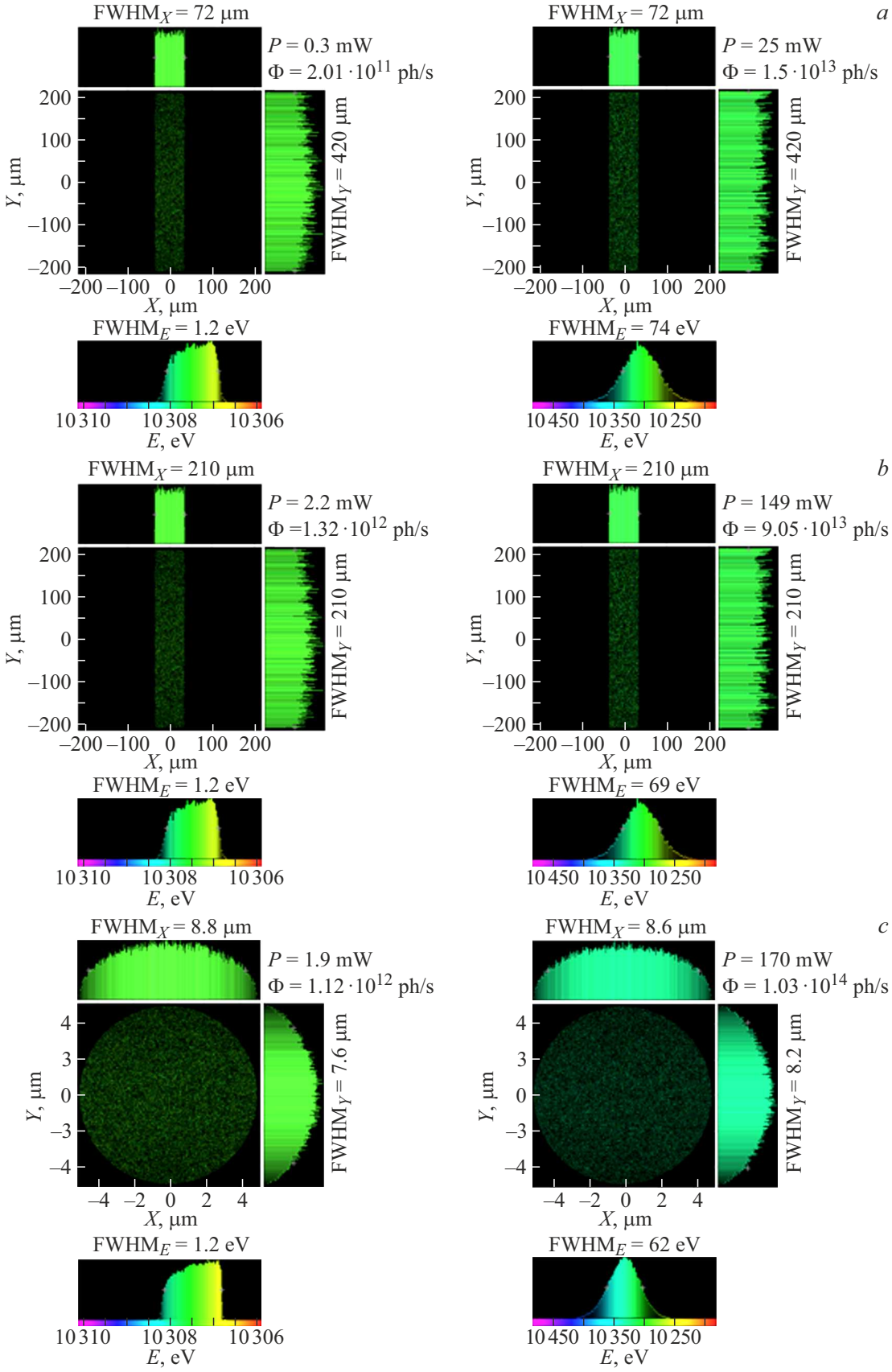

Figure 6. Radiation parameters on the specimen: *a* — lensless mode, *b* — speckle microscopy mode with secondary source; *c* — „coarse“ scanning. Left-hand figures correspond to the DMM and DCCM case, right-hand figures correspond only to the DMM case.

Table 3. Thermal loads on the apertures for operation at 10.3 keV without DCCM

	FWHM horizontal spot size, μm	FWHM vertical spot size, μm	Power, W	Peak density of power, W/mm^2
Slit at 69.5 m; without lenses	2170	3840	7.5	1
Pinhole at 70 m; focusing mode 1:1	80	16.3	3.4	2200
Pinhole at 52.5 m; modes with secondary source	40	9	3	6100

The calculation is performed by the raytracing method in xrt software[26].

The nanofocusing mode uses crossed adiabatically focusing lenses that achieve the diffraction limit — geometrical aperture of the lenses is lower than $l^{(trans)} = 210\,\mu$m, therefore the focal spot size corresponds to the Airy disk diameter.

$$2q = \frac{1.22\lambda}{\mathrm{NA}} \sim 100\,\mathrm{nm}.$$

When used at higher undulator harmonics, sub-100 nm focusing is available.

A pair of crossed multilayer Laue lenses may serve as an alternative for nanofocusing. In [27], such lenses with NA $\approx 8 \cdot 10^{-3}$ at 16.3 keV were used to achieve experimentally the focal spot sizes of < 10 nm on both axes.

10. Specimen positioning system and detectors

The detection diagram is shown in Figure 7. The specimen may move in two coordinates in the vertical plane inclined at 45° to the SR beam and also rotate about the vertical axis in the tomography mode. An energy-dispersive detector receiving the fluorescent signal is placed near the specimen at right angle to the SR beam and at 45° to the specimen motion plane. X-ray fluorescence (XRF) analysis, if required, may be performed using the confocal arrangment [28]. In the speckle microscopy mode, a pixelated $2D$ detector recording near-field diffraction patterns is placed at ~ 1 m from the specimen. In the ptychography mode, $2D$-detector is moved at 5–10 m from the specimen to record far-field diffraction patterns. The described arrangement is used for specimen mapping by the ptychography and XRF microspectroscopy methods simultaneously.

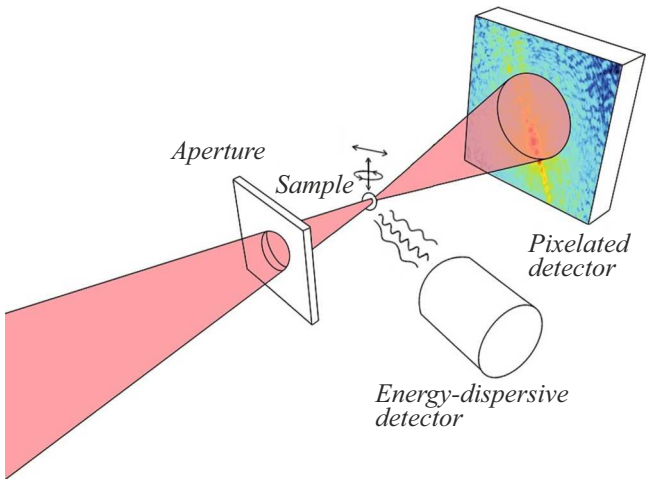

Figure 7. Detection diagram.

Conclusion

Optical arrangement of the fourth-generation SR source beamline for hard X-ray coherent high-resolution microscopy and microtomography has been proposed. The paper describes operation modes of optics that are used to vary the scale of the area of interest within $\sim 0.1-100\,\mu$m and achieve the spatial resolution of ~ 10 nm. Features of optics used on beams with high coherent flux fraction, including those that neutralize the disadvantages of beryllium lenses, are shown.

Acknowledgments

The authors are grateful to I.P. Dolbnya for consultation in the area of X-ray microscopy and beryllium lens applications. The authors are also grateful to E.I. Glushkov for provided data on multilayer structures and to A.V. Murzina for the assistance in preparing the illustrative material.

Funding

The study was performed under State assignment №2022-0006.

Conflict of interest

The authors declare that they have no conflict of interest.

References

[1] F. Pfeiffer. Nature Photonics, **12** (1), 9 (2018). DOI: 10.1038/s41566-017-0072-5

[2] N.L. Popov, I.A. Artyukov, A.V. Vinogradov, V.V. Protopopov. Phys. Usp., **63** (8), 766 (2020). DOI: 10.3367/UFNe.2020.05.038775
[3] Th. Roth, L. Helfen, J. Hallmann, L. Samoylova, P. Kwaśniewski, B. Lengeler, A. Madsen. SPIE, **9207**, 920702 (2014). DOI: 10.1117/12.2061127
[4] I. Lyatun, P. Ershov, I. Snigireva, A. Snigirev. J. Synchrotron Radiation, **27** (1), 44 (2020). DOI: 10.1107/S1600577519015625
[5] U. Johansson, D. Carbone, S. Kalbfleisch, A. Björling, M. Kahnt, S. Sala, T. Stankevic, M. Liebi, A. Rodriguez Fernandez, B. Bring, D. Paterson, K. Thånell, P. Bell, D. Erb, C. Weninger, Z. Matej, L. Roslund, K. Åhnberg, B. Norsk Jensen, H. Tarawneh, A. Mikkelsenc, U. Vogtd. J. Synchrotron Radiation, **28** (6), 1935 (2021). DOI: 10.1107/S1600577521008213
[6] H.C.N. Tolentino, M.M. Soares, C.A. Perez, F.C. Vicentin, D.B. Abdala, D. Galante, V. de C. Teixeira, D.H.C. de Araújo, H. Westfahl Jr. J. Physics: Conf. Series, **849** (1), 012057 (2017). DOI: 10.1088/1742-6596/849/1/012057
[7] S.J. Alloo, K.S. Morgan, D.M. Paganin, K.M. Pavlov. Scientif. Reports, **13** (1), 5424 (2023). DOI: 10.1038/s41598-023-31574-z
[8] K.M. Pavlov, H.(Th.) Li, D.M. Paganin, S. Berujon, H. Rougé-Labriet, E. Brun. Phys. Rev. Appl., **13** (5), 054023 (2020). DOI: 10.1103/PhysRevApplied.13.054023
[9] Zh. Qiao, X. Shi, Yu. Yao, M.J. Wojcik, L. Rebuffi, M.J. Cherukara, L. Assoufid. Optica, **9** (4), 391 (2022). DOI: 10.1364/OPTICA.453748
[10] P. Thibault, M. Dierolf, O. Bunk, A. Menzel, F. Pfeiffer. Ultramicroscopy, **109** (4), 338 (2009). DOI: 10.1016/j.ultramic.2008.12.011
[11] H. Wang, S. Berujon, J. Herzen, R. Atwood, D. Laundy, A. Hipp, K. Sawhney. Scientif. Reports, **5** (1), 8762 (2015). DOI: 10.1038/srep08762
[12] M. Dierolf, A. Menzel, P. Thibault, Ph. Schneider, C.M. Kewish, R. Wepf, O. Bunk, F. Pfeiffer. Nature, **467** (7314), 436 (2010). DOI: 10.1038/nature09419
[13] A.V. Akimov, Yu.S. Aktershev, V.V. Anashin, A.V. Andiyanov, O.V. Anchugov, M.V. Arcentyeva, P.A. Bak, G.N. Baranov, A.M. Barnyakov, A.M. Batrakov, O.V. Belikov, L.L. Belova, E.A. Bekhtenev,V.I. Bukhtiyarov, A.V. Bogomyakov, V.M. Borin, D.B. Burenkov, D.S. Vinnik, V.N. Volkov, E.S. Vonda, K.M. Gorchakov, K.A. Grishina, D.S. Gurov, G.A. Gusev, B.A. Dovzhenko, E.N. Dementyev, A.I. Erokhin, A.A. Zharikov, K.V. Zhilyaev, A.A. Zhukov, A.N. Zhuravlev, K.V. Zolotarev, N.A.Zolotukhina, Ya.V. Zubavichus, S.E. Karnaev, G.V. Karpov, K.Yu. Karyukina, V.D. Kashkin, V.A. Kiselev, V.V. Kobets, E.S. Kotov, V.Ya Korchagin, A.A. Krasnov, V.S. Krapivin, S.A. Krutikhin, V.S. Kuzminykh, G.N. Kulipanov, I.V. Kuptsov, G.Ya Kurkin, A.E. Levichev, E.B. Levishev, D.V. Leshonok, (Dorokhova), P.V. Logachev, Yu.I. Maltseva, Ma syao Chao, N.A. Mezentsev, O.I. Meshkov, N.V. Mityanina, I.A. Morozov, A.A.Morsin, S.A. Nikitin, D.A. Nikiforov, B.K. Ovchar, I.N. okunev, A.V. Pavlenko, O.A. Pavlov, A.Yu Pakhomov, V.M. Petrov, S.L. Pivovarov, P.A. Piminov, A.V. Polyansky, D.N. Pureskin, D.F. Reshetov, V.V. repkov, E.A. Rotov, T.V. Rybitskaya, S.L. Samoilov, I.K. Sedlyarov, A.M. Semenov, D.V. Sen'kov, L.E. Serdakov, Sh.R. Signatulin, S.V. Sinyatkin, M.A. Skamarokha, A.A. Starostenko, A.G. Tribendis, A.V. Utkin, M.G. Fedotov, A.S. tsyganov, A.D. Shiyankov, D.A. Shvedov, V.A. Shkaruba,K.S. Shtro, N.S. Shchegolkov. Tekhnologicheskaya infrastruktura sibirskogo kol'tsevogo istichnika fotonov SKIF, **2**, 98 (2022). (in Russian)
[14] V.A. Shkaruba, A.V. Bragin, A.A. Volkov, A.I. Erokhin, A.V. Zorin, F.P. Kazantsev, P.V. Kanonik, N.A. Mezentsev, A.N. Safronov, A.A. Sedov, O.A. Tarasenko, S.V. Khrushchev. Phys. Part. Nucl. Lett., **20** (4), 904 (2023). DOI: 10.1134/S1547477123040623
[15] N.I. Chkhalo, M.N. Drozdov, E.B. Kluenkov, A.Ya. Lopatin, V.I. Luchin, N.N. Salashchenko, N.N. Tsybin, L.A. Sjmaenok, V.E. Banine, A.M. Yakunin. J. Micro/Nanolithography, MEMS, MOEMS, **11** (2), 021115 (2012). DOI: 10.1117/1.jmm.11.2.021115
[16] T. Tanaka. J. Synchrotron Radiation, **28** (4), 1267 (2021). DOI: 10.1107/S1600577521004100
[17] E.I. Glushkov, I.V. Malyshev, E.V. Petrakov, N.I. Chkhalo, Yu.V. Khomyakov, Ya.V. Rakshun, V.A. Chernov, I.P. Dolbnya. J. Surf. Investig., **17** (1), 233 (2023). DOI: 10.1134/S1027451023070133
[18] R. Pleshkov, N. Chkhalo, V. Polkovnikov, M. Svechnikov, M. Zorina. J. Appl. Crystallography, **54** (6), 1747 (2021). DOI: 10.1107/S160057672101027X
[19] V.A. Chernov, I.A. Bataev, Ya.V. Rakshun, Yu.V. Khomyakov, M.V. Gorbachev, A.E. Trebushinin, N.I. Chkhalo, D.A. Krasnorutskiy, V.S. Naumkin, A.N. Sklyarov, N.A. Mezentsev, A.M. Korsunsky, I.P. Dolbnya. Rev. Scientif. Instruments, **94** (1), 013305 (2023). DOI: 10.1063/5.0103481
[20] Th. Bigault, E. Ziegler, Ch. Morawe, R. Hustache, J.-Y. Massonnat, G. Rostaing. Crystals, Multilayers, and Other Synchrotron Optics. — SPIE, **5195**, 12 (2003). DOI: 10.1117/12.515980
[21] H. Liang, W.F. Sheng, H. Shi, Y.M. Yang, L.R. Zheng. Synchrotron Radiation, **21**, 315 (2014). DOI: 10.18429/JACoW-MEDSI2020-TUPA08
[22] J. Patommel, S. Klare, R. Hoppe, S. Ritter, D. Samberg, F. Wittwer, A. Jahn, K. Richter, Ch. Wenzel, J.W. Bartha, M. Scholz, F. Seiboth, U. Boesenberg, G. Falkenberg, Ch.G. Schroer. Appl. Phys. Lett., **110** (10), 101103 (2017). DOI: 10.1063/1.4977882
[23] V.P. Nazmov, E.F. Reznikova, A. Somogyi, Ju. Mohr, V. Saile. Design Microfabrication of Novel X-Ray Optics II. — SPIE, **5539**, 235 (2004). DOI: 10.1117/12.562615
[24] K.S. Morgan, D.M. Paganin, K.K.W. Siu. Appl. Phys. Lett., **100** (12), 124102 (2012). DOI: 10.1063/1.3694918
[25] M.-Ch. Zdora, P. Thibault, F. Pfeiffer, I. Zanette. J. Appl. Phys., **118** (11), 113105 (2015). DOI: 10.1063/1.4931145
[26] K. Klementiev, R. Chernikov. Advances in Computational Methods for X-ray Optics III. — SPIE, **9209**, 60 (2014). DOI: 10.1117/12.2061400
[27] S. Bajt, M. Prasciolu, H. Fleckenstein, M. Domaracký, H.N. Chapman, A.J. Morgan, O. Yefanov, M. Messerschmidt, Ya. Du, K.T. Murray, V. Mariani, M. Kuhn, S. Aplin, K. Pande, P. Villanueva-Perez, K. Stachnik, J.P.J. Chen, A. Andrejczuk, A. Meents, A. Burkhardt, D. Pennicard, Xi. Huang, H. Yan, E. Nazaretski, Yo. Chu, Ch.E. Hamm. Light: Sci. Applicat., **7** (3), 17162 (2018). DOI: 10.1038/lsa.2017.162
[28] F.A. Daryin. *Razvitie metoda konfokal'noy rentgenovskoy mikrosckopii dlya issledovaniya mikrovklyucheniy v razlichnye geologicheskie matritsy* (Diss. kand. tekh. nauk. Institute yadernoy fiziki im G.I. Budkera SO RAN, Novosibirsk, 2022), 141 s. (in Rusian)

Translated by E.Ilinskaya